Vibration and Wave Propagation Control of Plates with Periodic Arrays of Shunted Piezoelectric Patches

A. Spadoni, M. Ruzzene and K. Cunefare

Journal of Intelligent Material Systems and Structures 2009; 20; 979 originally published online Mar 16, 2009;
DOI: 10.1177/1045389X08100041

Vibration and Wave Propagation Control of Plates with Periodic Arrays of Shunted Piezoelectric Patches

A. Spadoni,[1] M. Ruzzene[1,*] and K. Cunefare[2]

[1]*School of Aerospace Engineering, Georgia Institute of Technology, Atlanta GA, 30332, USA*

[2]*School of Mechanical Engineering, Georgia Institute of Technology, Atlanta GA, 30332, USA*

ABSTRACT: Periodic arrays of shunted, piezoelectric patches are employed to control waves propagating over the surface of plate structures, and corresponding vibrations. The shunted, piezoelectric patches act as sources of impedance mismatch, which gives rise to interference phenomena resulting from the interaction between incident, reflected and transmitted waves. Periodically distributed mismatch zones, i.e., the piezo patches, produce frequency dependent, wave-dynamic characteristics, which include the generation of band gaps, or stop bands in the frequency domain. The extent of induced band gaps depends on the mismatch in impedance generated by each patch. The total impedance mismatch, in turn, is determined by the added mass and stiffness of each patch as well as the shunting electrical impedance. Proper selection of the shunting electric-circuit thus provides control over the attenuation capabilities of the piezo-plate structure, as well as the ability to adapt to changing excitation conditions. Control of wave-propagation attenuation and vibration reduction for plates with periodic, shunted, piezoelectric patches is demonstrated numerically, employing finite-element models of the considered structures.

Key Words: piezoelectric patches, waves propagation shunted circuits, stop bands, periodicity.

INTRODUCTION

The application of shunted, piezoelectric materials for vibration control has received great attention by the structural dynamics community. Such passive vibration control strategy relies on the conversion of mechanical energy, associated to vibrations, into electrical energy, dissipated through a passive electrical circuit. The concept has been first introduced by Forward (1979) and then subsequently developed in the seminal paper by Hagood and Von Flotow (1991b) where it is applied to the vibration control of a cantilever beam. An elegant description of the concept shows how the piezo and shunting circuit introduce an additional degree of freedom in the system, which essentially acts as a tuned vibration absorber. The impedance of an RLC circuit may be selected to maximize energy conversion at the circuit's resonance frequency, so that energy conversion and dissipative effects on the structure are optimized. Similarly to a tuned vibration absorber, electromechanical damping through RLC-shunting occurs over a very narrow frequency band, so that tuning must be performed by carefully targeting single structural modes. Various other researchers have investigated ways to increase effectiveness over broader frequency ranges through alternative, more complex shunting strategies (see for example Tang and Wang, 1999b; Behrens and Moheimani, 2000; Clark, 2000; Behrens et al., 2002). Noteworthy is the multi-modal shunting approach presented by Hollkamp (1994), which considers shunting circuits with multiple resonant branches tuned at frequencies corresponding the modes of the structure to be damped. Similar concepts proposing refinements to reduce the coupling between the circuit branches can be found in papers by Wu (1999); Corr and Clark (2001); Moheimani et al. (2001); Moheimani and Behrens (2004). More recently, negative impedance circuits proposed for example in Morgan and Wang (2000); Park and Baz (2005); Neubauer and Oleskiewicz, (2006), have shown excellent broadband capabilities, but careful circuit design is required to avoid inducing instability in the system.

This article presents a different approach, where a periodic array of shunted piezo-patches is mounted on a plate to control the propagation of elastic waves, and the subsequent onset of vibrations. The patches represent sources of impedance mismatch, partially reflecting the propagating waves. The interference among incident, reflected and transmitted waves at the discontinuity zones can be constructive or destructive, depending on the wavelength and therefore on the frequency of the waves. Periodically induced impedance-mismatch zones

*Author to whom correspondence should be addressed.
E-mail: massimo.ruzzene@ae.gatech.edu
Figures 1–5 and 8 appear in color online: http://jim.sagepub.com

1045-389X/09/08 0979–12 $10.00/0 DOI: 10.1177/1045389X08100041

generate frequency bands where waves are free to propagate along the structure (pass bands), and frequency bands where waves are attenuated (stop bands) (Mead, 1996). The tunable characteristics of shunted, piezoelectric materials (Hagood and Von Flotow, 1991a) allow for the equivalent mechanical impedance of the patch to be tuned so that stop bands are generated over desired frequency ranges. In addition, the energy-dissipation characteristics of shunted, piezoeletric patches can be utilized to dampen the amplitude of vibration outside the stop bands. The proposed treatment, therefore, combines several concepts for vibration suppression, such as wave attenuation through destructive interference, and structural damping. The concept has been previously demonstrated on 1D rods and axisymmetric shells (Thorp et al., 2001, 2005) and it is here extended to flat plates. The approach considers multiple shunting patches following a method that was previously investigated for vibration confinement and vibration de-localization in rotationally periodic structures (Tsai and Wang, 1996; Tang and Wang, 1999a, 2003). The use of more than one patch to damp a relatively large number of modes is discussed by Moheimani et al. (2004). Moreover, the technique presented in this article can be considered as slightly different since the spatial periodicity of the patches is exploited to generate a frequency band where waves are attenuated, and resulting vibrations are reduced, without specifically targeting the modes of the structure.

The analysis is carried out employing a finite-element (FE) model which is formulated to account for the effects of the shunted piezos, and allows the prediction of the dispersion relations for the plate-piezo-patch system through the unit-cell-analysis approach, typically used to investigate wave propagation in periodic structures.

The article is organized in six sections and one appendix. This introduction (first section) is followed by the description of the Finite Element formulation for structures with shunted piezo patches (second section), while Section three summarizes the fundamentals of the technique used to analyze the propagation of waves in 2D periodic structures. The analysis is applied to plates with periodic piezo patches as described in Section three, and verified in Section five through the prediction of the harmonic response of finite plates with shunted arrays. Finally Section six summarizes the main results of the work and provides recommendation for future research.

FINITE ELEMENT FORMULATION

General Description

The formulation, within a general FE framework, for the analysis of structures with piezoelectric patches begins with the definition of the well-known constitutive equations for a piezoelectric material (Becker et al., 2006):

$$\begin{aligned} \boldsymbol{\sigma} &= [c]^E \boldsymbol{\varepsilon} - [e]^\sigma \boldsymbol{E}, \\ \boldsymbol{D} &= [e]\boldsymbol{\varepsilon} + [\varepsilon]^\varepsilon \boldsymbol{E}, \end{aligned} \tag{1}$$

where $\boldsymbol{\sigma} = \{\sigma_x\ \sigma_y\ \sigma_z\ \tau_{xz}\ \tau_{yz}\ \tau_{xy}\}^T$ and $\boldsymbol{\varepsilon} = \{\varepsilon_x\ \varepsilon_y\ \varepsilon_z\ \gamma_{xz}\ \gamma_{yz}\ \gamma_{xy}\}^T$ respectively are the mechanical stress and strain vectors, $\boldsymbol{D} = \{D_x\ D_y\ D_z\}^T$ is the electric charge vector, and $\boldsymbol{E} = E_x\, E_y\, E_z\}^T$ is the electric field vector. Also, $[c]^E$, $[e]^\sigma$, and $[\varepsilon]^\varepsilon$ denote the mechanical stiffness matrix at constant electric field, the piezoelectric stress coupling matrix evaluated at constant stress, and the permittivity matrix at constant strain. In the adopted notation convention, lower case bold letters indicate vectors, while matrices are denoted with capital bold letters, or using square brackets.

The formulation of governing equations for the piezoelectric medium, and the subsequent FE discretization are based on the expressing the total potential for a volume V of piezoelectric material:

$$\begin{aligned} \Pi = \frac{1}{2}\int_V \rho \dot{\boldsymbol{u}}^T \dot{\boldsymbol{u}}\ \mathrm{d}V + \frac{1}{2}\int_V \boldsymbol{\varepsilon}^T \boldsymbol{\sigma}\ \mathrm{d}V + \int_V \boldsymbol{\varepsilon}^T \boldsymbol{\sigma}_p\ \mathrm{d}V \\ - \frac{1}{2}\int_V \mathbf{E}^T \boldsymbol{D}_e\ \mathrm{d}V - W_e, \end{aligned} \tag{2}$$

where $\mathbf{u}$ is the displacement vector for the solid, $\boldsymbol{\sigma}_P$ is the mechanical stress vector due to piezoelectric effects produced by an electric field, $\boldsymbol{D}_e$ is the electric charge vector due to the presence of an electric field, and W_e is the work done by external forces. Electro-elastic matrix relations for a finite element are obtained by expressing continuous displacements, strains and electric potentials in terms of nodal values through a proper set of interpolation functions and their derivatives (Cook et al., 2007):

$$\begin{aligned} \boldsymbol{u} &= \boldsymbol{N}\boldsymbol{d}, \\ \boldsymbol{\varepsilon} &= \boldsymbol{B}_u \boldsymbol{d}, \\ \boldsymbol{E} &= -\boldsymbol{B}_\phi \phi, \end{aligned} \tag{3}$$

where $\boldsymbol{N}$ is the matrix of the shape functions, $\boldsymbol{B}_u$ is the strain interpolation matrix, while $\boldsymbol{B}_\phi$ is the electric field interpolation matrix. Equilibrium is imposed by enforcing that the total potential be at a minimum:

$$\delta\Pi = 0 \tag{4}$$

Substituting Equation (3) into Equation (2), and enforcing Equation (4) leads to the following electro-elastic system of equations governing the behavior of the considered piezoelectric-elastic domain:

$$\begin{aligned} \boldsymbol{M}_{uu}\ddot{\boldsymbol{d}} + \boldsymbol{K}_{uu}\boldsymbol{d} + \boldsymbol{K}_{u\phi}\phi = \boldsymbol{f}, \\ \boldsymbol{K}_{\phi u}\boldsymbol{d} + \boldsymbol{K}_{\phi\phi}\phi = \boldsymbol{q}, \end{aligned} \tag{5}$$

where the structural mass and stiffness matrices are, respectively, defined as:

$$\boldsymbol{M}_{uu} = \int_V \rho \boldsymbol{N}^T \boldsymbol{N} \, \mathrm{d}V, \tag{6}$$

and

$$\boldsymbol{K}_{uu} = \int_V \boldsymbol{B}_u^T \boldsymbol{C} \boldsymbol{B}_u \, \mathrm{d}V. \tag{7}$$

The dielectric stiffness matrix $\boldsymbol{K}_{\phi\phi}$ is:

$$\boldsymbol{K}_{\phi\phi} = \int_V \boldsymbol{B}_\phi^T \epsilon^\varepsilon \boldsymbol{B}_\phi \, \mathrm{d}V. \tag{8}$$

Finally, the piezoelectric stiffness matrix $\boldsymbol{K}_{u\phi} = \boldsymbol{K}_{u\phi}^T$ coupling the structural and electrical behavior of the system is given by:

$$\boldsymbol{K}_{u\phi} = \int_V \boldsymbol{B}_u^T \boldsymbol{e}^\sigma \boldsymbol{B}_\phi \, \mathrm{d}V. \tag{9}$$

Application to Plates with Shunted Patches

The formulation presented above is general and can be applied to any type of piezoelectric structure, given the proper FE formulation. In this work, such formulation is used to model thin plates (the host structure) on which shunted piezos are mounted. The combination of host structure and piezo patches is modeled using 4-node Kirchhoff plate elements (Cook et al., 2007). Piezoelectric patches are assumed to have through-the-thickness polarization, with electrodes connected to the top and bottom surfaces. Furthermore, it is assumed that no electric-field gradients are present on the top or bottom surface of each piezoelectric patch, producing iso-electric-potential surfaces. Accordingly, the electric potential, or voltage, varies only through the thickness of the piezo patches. Moreover, it is assumed that the variation of voltage through the thickness is linear, and that the bottom surface of each patch bonded to the host structure is grounded (Figure 1).

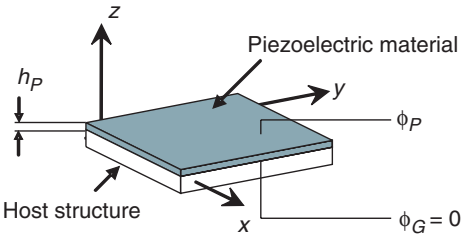

Figure 1. *Configuration of plate with piezo patch.*

The variation of voltage over the volume of the plate can thus be expressed as:

$$\phi(x, y, z) = \phi(z) = \frac{z - h/2}{h_P} \phi_P, \tag{10}$$

with h and h_P denoting the plate and the piezo thickness, respectively. Based on these assumptions, the governing electrical equation for a single piezo element (Equation (5)) becomes a scalar equation of the form:

$$\boldsymbol{K}_{\phi u} \boldsymbol{d} + K_{\phi\phi} \phi_P = q_e, \tag{11}$$

with the coupling matrix $\boldsymbol{K}_{\phi u} \in \mathbb{R}^1 \times \mathbb{R}^n$, with n denoting the number of structural degrees of freedom, and q_e being the external charge at the electrodes. The application of a shunting circuit through the electrodes allows expressing the charge in terms of the potential ϕ_P. Assuming harmonic motion at frequency ω, and correspondingly harmonic variation of voltage and charge, i.e.,

$$\phi_P = \phi_{P0} e^{i\omega t}, \quad q_e = q_{e0} e^{i\omega t} \tag{12}$$

gives:

$$\phi_{P0} = i\omega Z_e(\omega) q_{e0}, \tag{13}$$

where $Z_e(\omega)$ is the electrical impedance of the shunting circuit, which for the simple case of shunting through a series of an inductance L and a resistance R is $Z_e(\omega) = R + i\omega L$ (Figure 2).

Substituting Equation (13) into Equation (11) leads to the expression for the potential in terms of structural degrees of freedom, with a single governing matrix equation of the form:

$$[\boldsymbol{K}_{uu} - \omega^2 \boldsymbol{M}_{uu} + \boldsymbol{S}_{Z_e}(\omega)] \ \boldsymbol{d}_0 = \boldsymbol{f}_0, \tag{14}$$

where $\boldsymbol{S}_{Z_e}(\omega)$ is a structural shunting matrix containing the effects of the shunting circuits on the dynamic behavior of the structure. Its expression is:

$$\boldsymbol{S}_{Z_e}(\omega) = -i\omega \boldsymbol{K}_{u\phi} \left(i\omega K_{\phi\phi} - \frac{1}{Z_e(\omega)} \right)^{-1} \boldsymbol{K}_{\phi u}. \tag{15}$$

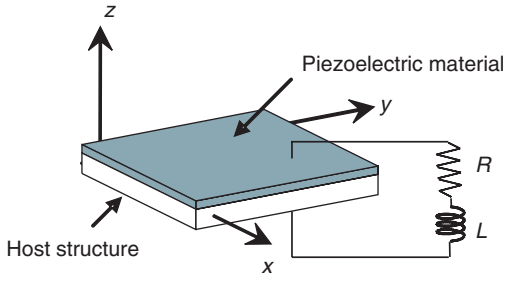

Figure 2. *Plate with shunted piezo patch.*

It is interesting to observe how the shunting matrix contributes to the inertial, damping and stiffness properties of the structure in ways that are defined by the characteristics of the piezo patch and by the parameters of the shunting circuit by way of the electrical impedance. Particular cases are those corresponding to the short and open shunting circuits, which correspond to limiting shunting conditions. The short circuit configuration, for which $\phi_P = 0$, is governed by the following discretized Equation of motion:

$$\left[\boldsymbol{K}_{uu} - \omega^2 \boldsymbol{M}_{uu}\right]\boldsymbol{d}_0 = \boldsymbol{f}_0, \tag{16}$$

where $\boldsymbol{M}_{uu}$ and $\boldsymbol{K}_{uu}$ include mass and stiffness of the piezoelectric patches, and of the host structure. The open circuit case corresponds to $Z_e(\omega) \to \infty$, which reduces the shunting matrix in Equation (15) to:

$$\boldsymbol{S}_{Z_e}(\omega) \approx -\boldsymbol{K}_{u\phi}\boldsymbol{K}_{\phi\phi}^{-1}\boldsymbol{K}_{\phi u}, \tag{17}$$

which shows that the open circuit essentially modifies the stiffness of the host-piezo structure.

WAVE PROPAGATION IN 2D PERIODIC STRUCTURES

Plate structures with a periodic array of shunted, piezo patches are now considered. Wave propagation in the resulting 2D periodic structure is investigated through the analysis of a unit cell, and the application of Bloch theorem (Brillouin, 1953). A schematic of the considered plate configuration and associated unit cell is shown in Figure 3.

The motion of the periodic domain, according to Bloch's theorem, may be expressed as follows:

$$\boldsymbol{w}(\boldsymbol{r}, \boldsymbol{n}) = \boldsymbol{w}_0 e^{\boldsymbol{\mu}\cdot\boldsymbol{r}}, \tag{18}$$

where $\boldsymbol{w}$ denotes the generalized displacement of point $\boldsymbol{r}$ belonging to the cell at location $\boldsymbol{n}$ within the assembly. Also, $\boldsymbol{w}_0$ describes the generalized displacements of a single cell, while $\boldsymbol{\mu} = \begin{bmatrix}\mu_x & \mu_y\end{bmatrix}$ is the vector of the propagation constants. The propagation constants are complex numbers $\mu_k = \delta_k + i\varepsilon_k$, $(k = x, y)$, whose real and imaginary parts are denote *attenuation* and *phase* constants, respectively. The propagation constants are equal to the wavenumber component in the direction of wave propagation, multiplied by the spatial period of the domain in the corresponding direction (Figure 4), and therefore they are non-dimensional quantities. They describe the nature of elastic waves propagating in the 2D periodic structure: purely imaginary propagation constants correspond to waves which are free to propagate, while the existence of a real part indicates that amplitude attenuation occurs as elastic waves propagate from one cell to the next.

The behavior of the unit cell can be conveniently described through a discretized equation of motion, and by defining the cell's interaction with its neighbors. A general formulation for the cell's equation of motion can be expressed as:

$$\boldsymbol{K}_D(\omega)\boldsymbol{d} = \boldsymbol{f}, \tag{19}$$

where $\boldsymbol{K}_D$ is the dynamic stiffness matrix of the cell defined in Equation (14). In Equation (19) $\boldsymbol{d}$ and $\boldsymbol{f}$ are,

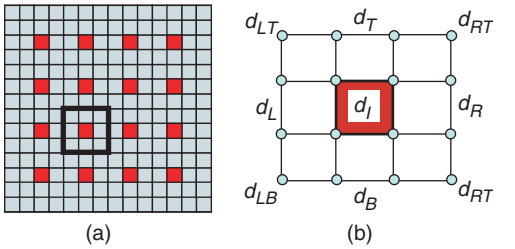

Figure 3. *(a) Schematic of the periodic plate; (b) Corresponding unit cell.*

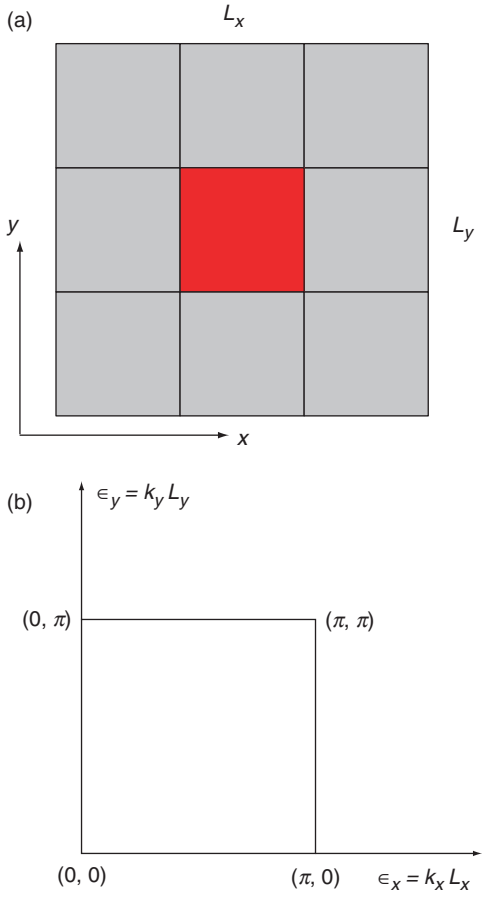

Figure 4. *(a) Unit cell dimensions; (b) First Irreducible Brillouin zone.*

respectively, vectors of generalized nodal displacements of the cell and associated forces:

$$\boldsymbol{d} = \{\boldsymbol{d}_L \quad \boldsymbol{d}_R \quad \boldsymbol{d}_T \quad \boldsymbol{d}_B \quad \boldsymbol{d}_{LB} \quad \boldsymbol{d}_{LT} \quad \boldsymbol{d}_{RT} \quad \boldsymbol{d}_{RB} \quad \boldsymbol{d}_I\}^T,$$
$$\boldsymbol{f} = \{\boldsymbol{f}_L \quad \boldsymbol{f}_R \quad \boldsymbol{f}_T \quad \boldsymbol{f}_B \quad \boldsymbol{f}_{LB} \quad \boldsymbol{f}_{LT} \quad \boldsymbol{f}_{RT} \quad \boldsymbol{f}_{RB} \quad \boldsymbol{f}_I\}^T,$$

where $\boldsymbol{d}_I$ and $\boldsymbol{f}_I$ denote the generalized displacements and forces internal to the unit cell. Imposing periodicity conditions on the generalized displacements and equilibrium conditions on the generalized forces yields:

$$\begin{aligned} &\boldsymbol{d}_R = e^{\mu_x}\boldsymbol{d}_L,\ \boldsymbol{d}_T = e^{\mu_y}\boldsymbol{d}_B, \\ &\boldsymbol{d}_{LT} = e^{\mu_y}\boldsymbol{d}_{LB},\ \boldsymbol{d}_{RB} = e^{\mu_x}\boldsymbol{d}_{LB}, \\ &\boldsymbol{d}_{RT} = e^{\mu_x+\mu_y}\boldsymbol{d}_{LB}, \end{aligned} \tag{20}$$

and

$$\begin{aligned} &\boldsymbol{f}_R = -e^{\mu_x}\boldsymbol{f}_L,\ \boldsymbol{f}_T = -e^{\mu_y}\boldsymbol{f}_B, \\ &\boldsymbol{f}_{LT} = -e^{\mu_y}\boldsymbol{f}_{LB},\ \boldsymbol{f}_{RB} = -e^{\mu_x}\boldsymbol{f}_{LB}, \\ &\boldsymbol{f}_{RT} = -e^{\mu_x+\mu_y}\boldsymbol{f}_{LB}. \end{aligned} \tag{21}$$

Equation's (20) and (21) can be rewritten in the following matrix form:

$$\boldsymbol{d} = \boldsymbol{A}\,\boldsymbol{d}^{(r)},\ \boldsymbol{f} = \boldsymbol{B}\boldsymbol{f}^{(r)}, \tag{22}$$

where $\boldsymbol{d}^{(r)}$ is the reduced vector of nodal displacements. Substituting Equation (20) into Equation (19), premultiplying the resulting Equations for $\boldsymbol{A}^H$, with H denoting a complex transpose conjugate, and assuming $\boldsymbol{f}_I = \boldsymbol{0}$ gives:

$$\boldsymbol{K}_D^{(r)}(\boldsymbol{\mu}, \omega)\,\boldsymbol{d}^{(r)} = \boldsymbol{0}, \tag{23}$$

where $\boldsymbol{K}_D^{(r)}(\boldsymbol{\mu}, \omega)$ is the reduced dynamic stiffness matrix. Equation (23) is an eigenvalue problem whose solution depends on the propagation constant $\boldsymbol{\mu}$.

Direct Solution of the Dispersion Relations

The approach typically used to evaluate the dispersion relation of a 2D periodic domain consists in setting the attenuation part of the propagation constants to 0, and varying the phase constants ε_i $(i = x, y)$ in the $[-\pi, \pi]$ interval. Solving with respect to frequency for all the combinations of ε_x, ε_y in the considered range yields a series of functions $\omega = f(\varepsilon_x, \varepsilon_y)$, which are known as *phase constant surfaces* and represent the dispersion characteristics of the domain. The phase constant surfaces are 2D representations of the dispersion relations for the considered periodic domain, and provide a wealth of information on the dynamics of propagating waves. Frequency gaps between subsequent surfaces correspond to attenuation in all directions and therefore identify the stop bands, or *band gaps*, typical of all periodic structures and domains. Phase constant surfaces are therefore essential tools for the analysis of the behavior of 2D periodic structures and their ability to transmit or attenuate waves at certain frequencies and in specified directions. This approach, here denoted as direct, is very convenient, as for most domains, specifying the two wavenumbers and solving for frequency leads to a linear eigenvalue problem of easy solution. This is, however, not the case for the configuration at hand. The reason for this is 2-fold: (1) the resistive component of the shunting circuit introduces attenuation at all frequencies, which does not allow setting the attenuation constants δ_k equal to 0, and (2) the dynamic stiffness matrix is a complicated function of frequency, so that even if the propagation constants were correctly specified, the resulting eigenvalue problem expressed by Equation (23) would not be linear with respect to frequency. The complexity is introduced by the electrical impedance, which appears as a factor on the denominator.

Inverse Solution of the Dispersion Relations: Transfer Matrix Technique

An alternative approach, here denoted as inverse, consists in specifying the frequency ω and one of the two wavenumbers, and solving for the other. This is performed by constraining the wave vector to follow the contour of the *First Brillouin Zone*, which is the area corresponding to one period of the frequency/wavenumber relationship. The *First Brillouin Zone* is identified by evaluating the inverse lattice for a periodic domain according to the procedure outlined in (Brillouin, 1953). Due to symmetry of the unit-cell configuration considered in this study, the *First Brillouin Zone* is a square defined by $[0, \pi] \times [0, \pi]$ as shown in Figure 4. The analysis through variation of the wave vector along the contour significantly reduces the computational effort in determining the dispersion surfaces, and in general, provides a representation of easy interpretation. The inverse solution method adopted here allows imposing the frequency, and one of the two wavenumbers and solving for the other wavenumber along each side of the contour.

This is achieved by extending the transfer matrix technique, typically restricted to the analysis of 1D periodic structures, with the underlying restriction that the propagation constants are only obtained for combinations corresponding to the contour of the Brillouin zone. The procedure is here illustrated for the case when propagation along the x direction is investigated, which corresponds to the first side of the contour $((0, 0) - (\pi, 0)$ with $\mu_y = 0)$. In the procedure

described in what follows, the unknown is μ_x while frequency ω is an input parameter. The following periodicity conditions are enforced:

$$\begin{aligned} \boldsymbol{d}_T &= \boldsymbol{d}_B, \\ \boldsymbol{d}_{LT} &= \boldsymbol{d}_{LB}, \\ \boldsymbol{d}_{RT} &= \boldsymbol{d}_{RB}. \end{aligned} \tag{24}$$

This yields a reduced Equation of motion of the kind:

$$\boldsymbol{K}_D^{(r)}(\mu_y = 0, \omega)\, \boldsymbol{d}^{(r)} = \boldsymbol{f}^{(r)} \tag{25}$$

where $\boldsymbol{d}^r = \{\boldsymbol{d}_L \quad \boldsymbol{d}_{LB} \quad \boldsymbol{d}_B \quad \boldsymbol{d}_I \quad \boldsymbol{d}_R \quad \boldsymbol{d}_{RB}\}^T$, and $\boldsymbol{f}^r = \{\boldsymbol{f}_L \quad \boldsymbol{f}_{LB} \quad \boldsymbol{f}_B \quad \boldsymbol{f}_I \quad \boldsymbol{f}_R \quad \boldsymbol{f}_{RB}\}^T$. Given the considered direction of wave propagation, the reduced set of degrees of freedom can be organized into left ($\mathcal{L}$), $\boldsymbol{d}_\mathcal{L} = \{\boldsymbol{d}_L \quad \boldsymbol{d}_{LB}\}^T$, internal ($\mathcal{I}$) $\boldsymbol{d}_\mathcal{I} = \{\boldsymbol{d}_B \quad \boldsymbol{d}_I\}^T$, and right ($\mathcal{R}$) $\boldsymbol{d}_\mathcal{R} = \{\boldsymbol{d}_R \quad \boldsymbol{d}_{RB}\}^T$. Similar definitions hold for the vectors of generalized forces, with the distinction that, due to equilibrium considerations, the absence of externally applied forces and the considered periodicity conditions, $\boldsymbol{f}_\mathcal{I} = \boldsymbol{0}$. Accordingly, Equation (25) can be rewritten as follows:

$$\begin{aligned} \boldsymbol{K}_D^{(r)}(\mu_y = 0, \omega) \begin{Bmatrix} \boldsymbol{d}_\mathcal{L} \\ \boldsymbol{d}_\mathcal{I} \\ \boldsymbol{d}_\mathcal{R} \end{Bmatrix} &= \begin{bmatrix} \boldsymbol{\alpha}_{\mathcal{L},\mathcal{L}} & \boldsymbol{\alpha}_{\mathcal{L},\mathcal{I}} & \boldsymbol{\alpha}_{\mathcal{L},\mathcal{R}} \\ \boldsymbol{\alpha}_{\mathcal{I},\mathcal{L}} & \boldsymbol{\alpha}_{\mathcal{I},\mathcal{I}} & \boldsymbol{\alpha}_{\mathcal{I},\mathcal{R}} \\ \boldsymbol{\alpha}_{\mathcal{R},\mathcal{L}} & \boldsymbol{\alpha}_{\mathcal{R},\mathcal{I}} & \boldsymbol{\alpha}_{\mathcal{R},\mathcal{R}} \end{bmatrix} \begin{Bmatrix} \boldsymbol{d}_\mathcal{L} \\ \boldsymbol{d}_\mathcal{I} \\ \boldsymbol{d}_\mathcal{R} \end{Bmatrix} \\ &= \begin{Bmatrix} \boldsymbol{f}_\mathcal{L} \\ \boldsymbol{0} \\ \boldsymbol{f}_\mathcal{R} \end{Bmatrix} \end{aligned} \tag{26}$$

Equation (26) can be recast into transfer-matrix form through the condensation of the internal degrees of freedom and by imposing relations between left and right displacements and forces. This gives:

$$\begin{Bmatrix} \boldsymbol{d}_\mathcal{R} \\ \boldsymbol{f}_\mathcal{R} \end{Bmatrix} = \boldsymbol{T}(\mu_y = 0, \omega) \begin{Bmatrix} \boldsymbol{d}_\mathcal{L} \\ \boldsymbol{f}_\mathcal{L} \end{Bmatrix}, \tag{27}$$

where

$$\boldsymbol{T}(\mu_y = 0, \omega) = \begin{bmatrix} -\hat{\boldsymbol{\alpha}}_{\mathcal{L},\mathcal{R}}^{-1} \hat{\boldsymbol{\alpha}}_{\mathcal{L},\mathcal{L}} & \hat{\boldsymbol{\alpha}}_{\mathcal{L},\mathcal{R}}^{-1} \\ \hat{\boldsymbol{\alpha}}_{\mathcal{R},\mathcal{R}} (\hat{\boldsymbol{\alpha}}_{\mathcal{L},\mathcal{R}}^{-1} \hat{\boldsymbol{\alpha}}_{\mathcal{L},\mathcal{L}}) - \hat{\boldsymbol{\alpha}}_{\mathcal{R},\mathcal{L}} & -\hat{\boldsymbol{\alpha}}_{\mathcal{R},\mathcal{R}}^{-1} \hat{\boldsymbol{\alpha}}_{\mathcal{L},\mathcal{R}} \end{bmatrix}, \tag{28}$$

with

$$\begin{aligned} \hat{\alpha}_{\mathcal{L},\mathcal{L}} &= \alpha_{\mathcal{L},\mathcal{L}} - \alpha_{\mathcal{L},\mathcal{I}} \alpha_{\mathcal{L},\mathcal{L}}^{-1} \alpha_{\mathcal{I},\mathcal{L}}, \\ \hat{\alpha}_{\mathcal{L},\mathcal{R}} &= \alpha_{\mathcal{L},\mathcal{R}} - \alpha_{\mathcal{L},\mathcal{I}} (\alpha_{\mathcal{I},\mathcal{I}}^{-1} \alpha_{\mathcal{I},\mathcal{R}}), \\ \hat{\alpha}_{\mathcal{R},\mathcal{L}} &= \alpha_{\mathcal{R},\mathcal{L}} - \alpha_{\mathcal{R},\mathcal{I}} (\alpha_{\mathcal{I},\mathcal{I}}^{-1} \alpha_{\mathcal{I},\mathcal{L}}), \\ \hat{\alpha}_{\mathcal{R},\mathcal{R}} &= \alpha_{\mathcal{R},\mathcal{R}} - \alpha_{\mathcal{R},\mathcal{I}} (\alpha_{\mathcal{L},\mathcal{L}}^{-1} \alpha_{\mathcal{I},\mathcal{R}}). \end{aligned}$$

The eigen values of the transfer matrix $\boldsymbol{T}(\mu_y = 0, \omega)$ can be obtained through the solution of the following eigenvalue problem:

$$\boldsymbol{T}(\mu_y = 0, \omega) \begin{Bmatrix} \boldsymbol{d}_\mathcal{L} \\ \boldsymbol{f}_\mathcal{L} \end{Bmatrix} = \lambda(\mu_y = 0, \omega) \begin{Bmatrix} \boldsymbol{d}_\mathcal{L} \\ \boldsymbol{f}_\mathcal{L} \end{Bmatrix} \tag{29}$$

Combining Equations (27) and (29) gives:

$$\begin{Bmatrix} \boldsymbol{d}_\mathcal{R} \\ \boldsymbol{f}_\mathcal{R} \end{Bmatrix} = \lambda(\mu_y = 0, \omega) \begin{Bmatrix} \boldsymbol{d}_\mathcal{L} \\ \boldsymbol{f}_\mathcal{L} \end{Bmatrix} \tag{30}$$

which indicates that the state vectors at the left and right of the unit cell identified by the particular direction of wave propagation are related through the eigenvalues of the transfer matrix. The eigenvalues therefore determine the nature of the wave dynamics in the periodic structure. Waves are free to propagate in the specified direction for those values of frequency for which $|\lambda| = 1$, whereas attenuation occurs if $|\lambda| < 1$. The propagation constant μ_x corresponding to the assigned value of frequency ω and to $\mu_y = 0$ can be obtained by letting:

$$\lambda = e^{\mu_x} \tag{31}$$

which is an expression that yields both imaginary and real part of the propagation constant. This procedure, described here ($(0,0) - (\pi, 0)$ with $\mu_y = 0$), can be replicated for the values of the propagation constants defining the other three sides of the Brillouin zone. The description of the periodicity conditions corresponding to the other sides, and the definition of the left, right, and internal degrees of freedom is provided in the Appendix.

WAVE PROPAGATION CHARACTERISTICS OF PLATES WITH SHUNTED PIEZOS

Unit Cell Configuration, Geometry, and Material Properties

The unit cell analysis presented in the previous section is now employed to investigate the propagation characteristics in the considered periodic plate-piezo-patch configurations. The analysis is performed for the two unit cells presented in Figure 5. For both cases, the host structure is made of aluminum (Young's Modulus $E = 7.1 \times 10^{10}\,\mathrm{N/m^2}$, density $\rho = 2700\,\mathrm{kg/m^3}$, Poisson's ratio $\nu = 0.33$) and has a thickness $h = 1\,\mathrm{mm}$. Both unit cells feature side lengths $L_x = L_y = 7.5\,\mathrm{cm}$. The considered piezo patch has a thickness $h = 0.5\,\mathrm{mm}$ and its properties are listed in Table 1. Both configurations are considered to be shunted through an RL circuit which is in series with the capacitance of the piezo. For the selected configuration this capacitance is equal to

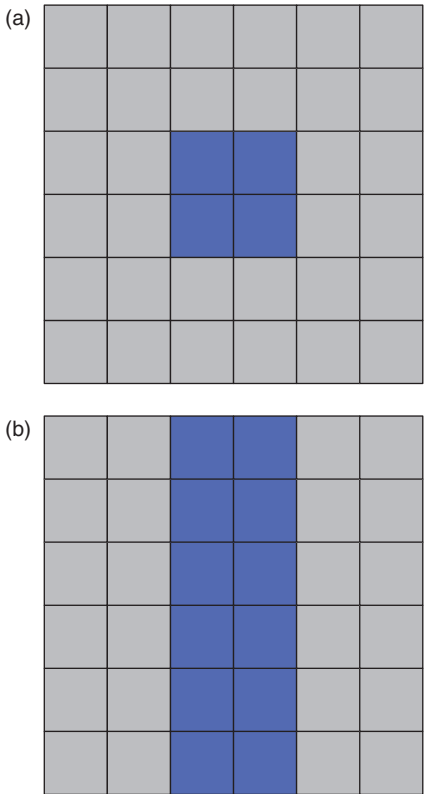

Figure 5. *Considered unit cell configurations.*

Table 1. Summary of properties of the piezo patches.

ρ_s	7700 kg/m^3
$c_{11}^E = c_{22}^E = c_{33}^E$	110.7 GPa
$c_{44}^E = c_{55}^E = c_{66}^E$	25.6 GPa
$c_{12}^E = c_{13}^E = c_{23}^E$	59.6 GPa
$e_{31} = e_{32}$	−9.6 N/Vm
$\epsilon_{33}^T/\epsilon_0$	2100
k_{31}	0.31

$C_P = 21\,n$F. The inductance of the circuit is chosen in order to tune the shunting circuit at its resonant frequency, which, in the absence of resistance, is given by:

$$\omega_{\text{TUN}} = \frac{1}{(\text{LC}_P)^{1/2}}. \tag{32}$$

Propagation Constant Results

Results for the first configuration (Figure 5(a)) are presented in Figure 6, which show the variation of the real (δ) and imaginary part (ϵ) of the propagation constants over the $0 - 1500$ Hz range. The results obtained with the shunted piezo are compared with the case of open circuit ($Z_E \to \infty$) which is presented as a limiting case. The propagation constants along the x-direction shown in Figure 6(a) and (b) show the presence of an attenuation frequency range centered at 450 Hz, which occurs for all circuit configurations. The presence of this attenuation band can be attributed to the impedance mismatch generated by the added mass and stiffness of the piezo. In addition, shunting of the circuits introduces an additional range of attenuation at approximately the tuning frequency, which in this case is set at 200 Hz, as defined by a shunting inductance $L = 30.14$ H. Another interesting observation is that the propagation constants along the x direction are identical to those along the y direction, as a result of the same spatial periodicity in both in-plane directions (Figure 5(a)).

The results for the second unit-cell configuration (Figure 5(b)) are presented in Figure 7, where propagation constants obtained for a tuning frequency of 700 Hz are displayed. As in the previous case, attenuation zones are identified by the range of frequencies where the attenuation constant δ is non-zero. The presence of an attenuation zone centered approximately at 450 Hz, for waves propagating in the x-direction (Figure 7(a)), is to be attributed to the impedance mismatch associated with the presence of the piezo-patch, as for the first configuration. This range of attenuation is in fact independent from the tuning frequency of the resonant shunts and is not observed in the propagation constant for the y-direction (Figure 7(c)), along which the configuration of Figure 5(b) does not feature any spatial periodicity.

The magnitude of the resistive component in the shunting circuit, moreover, affects the amplitude of the attenuation parameters and the frequency bandwidth of attenuation. Higher resistance values typically reduce the maximum attenuation value, but tend to extend the range of effectiveness. This suggests that a balance must be struck to achieve a compromise between bandwidth and attenuation amplitude. Such a behavior may be easily explained by observing that the shunting circuit under consideration behaves as a second-order system with a resonance at a frequency defined by inductance and capacitance, and a corresponding amplitude peak defined by the value of the resistance, here acting as the dissipative term. Maximum attenuation amplitude and bandwidth are concurrent and thus their dependence on resistance is here reported to illustrate the influence of various shunting circuits.

Finally, both Figures 6 and 7 illustrate how the attenuation zones are clearly identified by frequency ranges corresponding to non-zero attenuation parameter δ, while phase-constant plots are more difficult to interpret and do not provide clear information with respect to stop bands. For this reason, in the remainder of the article, only the attenuation constant plots will be reported as effective prediction tools for the range of effectiveness of the periodic arrangement of piezo-patches for vibration attenuation.

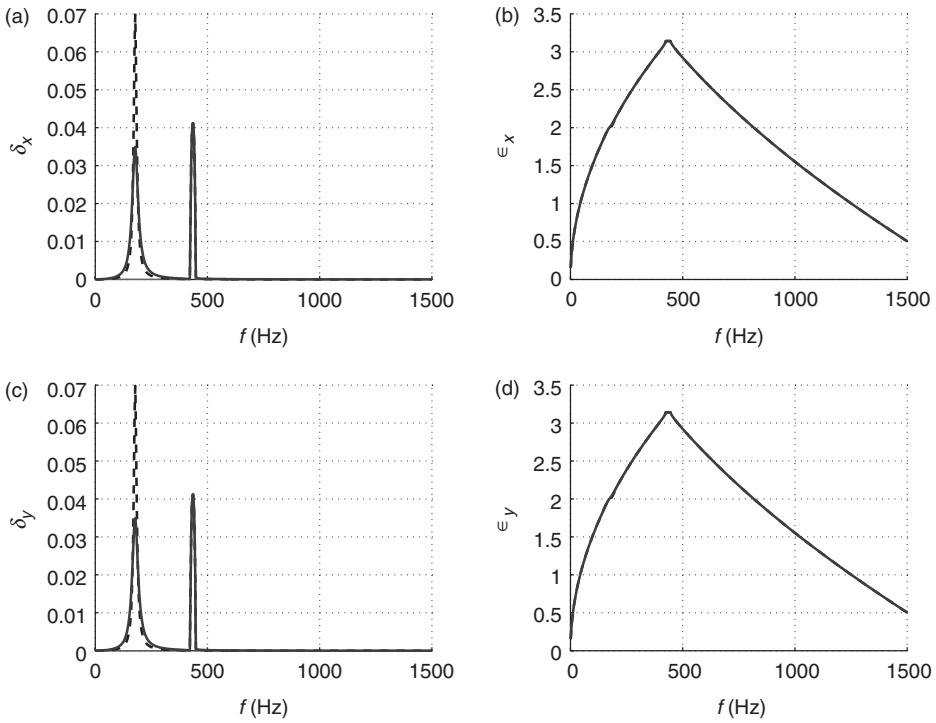

Figure 6. *Propagation constants for the first unit cell configuration tuned at 200 Hz: attenuation and phase constant along x (a,b), and along y (c,d) (L = 30.14 H; open circuit – thin solid line, R = 3000Ω – thick dashed line, R = 6000Ω – thick solid line).*

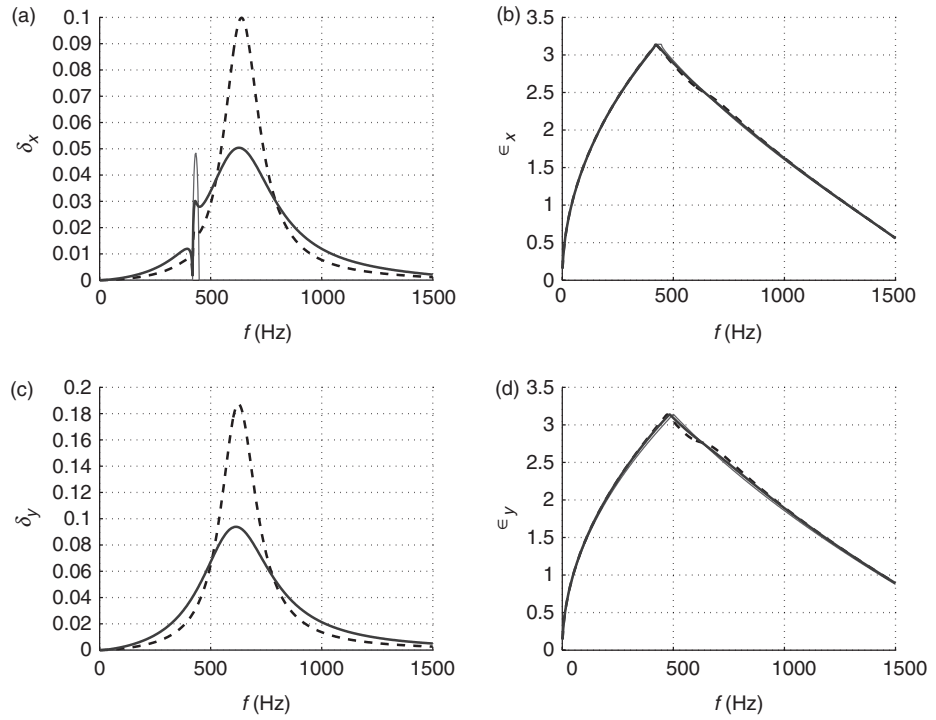

Figure 7. *Propagation constants for the first unit cell configuration tuned at 700 Hz: attenuation and phase constant along x (a,b), and along y (c,d) (L = 2.46 H; open circuit – thin solid line, R = 3000Ω – thick dashed line, R = 6000Ω – thick solid line).*

FREQUENCY RESPONSE OF A FINITE PLATE WITH A PERIODIC SHUNTED ARRAY

The predictions of the unit-cell analysis using Bloch theorem are verified by computing the harmonic response of a periodic plate of finite extent. The configuration under consideration, depicted in Figure 8, consists of an assembly of a 5×5 array of unit cells of the type shown in Figure 5(a). The considered material properties are those introduced in the previous section, while the modeled

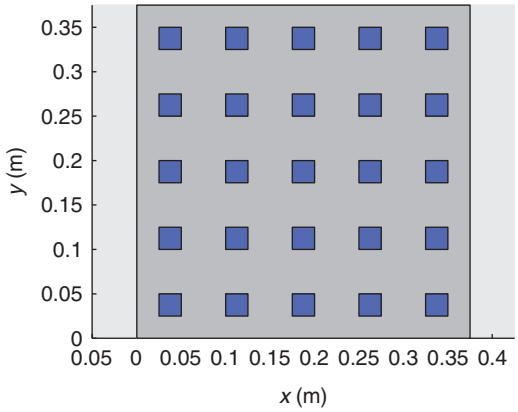

Figure 8. *Periodic plate configuration.*

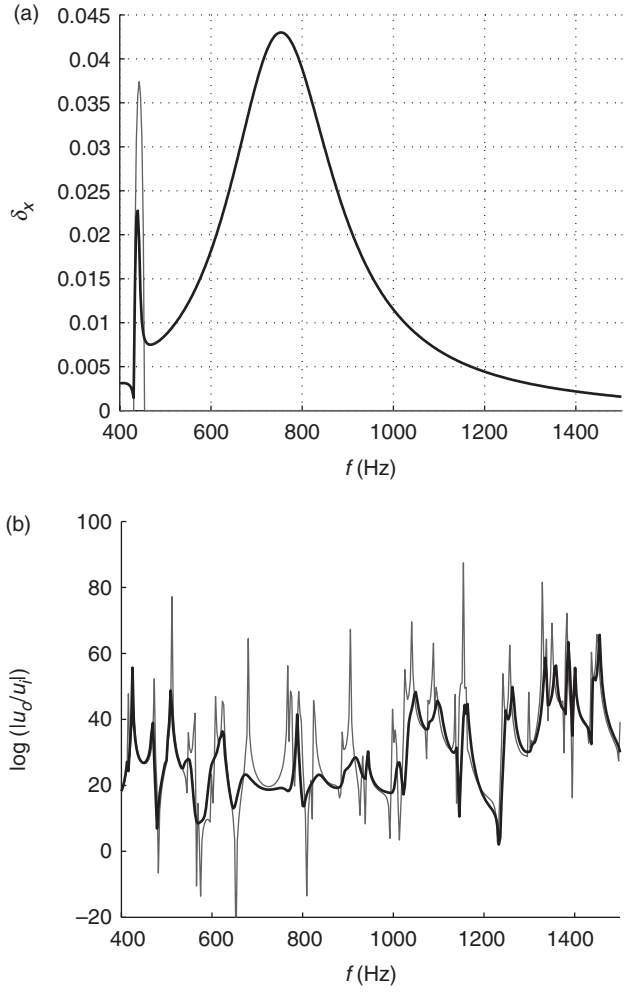

Figure 9. *Propagation constant (a) and frequency response function (b) with tuning at 850 Hz (tuning inductance L = 1.67 H): open circuit – thin solid line, shunting resistance R = 3000Ω – thick solid line.*

square plate features side lengths of 37.5 cm. The plate is assumed to have free–free boundary conditions, and to be excited by a harmonic displacement excitation at the bottom-left corner. The plate frequency response at the top-right corner is presented in Figures 9–12 for the open circuit case and for various shunting configurations.

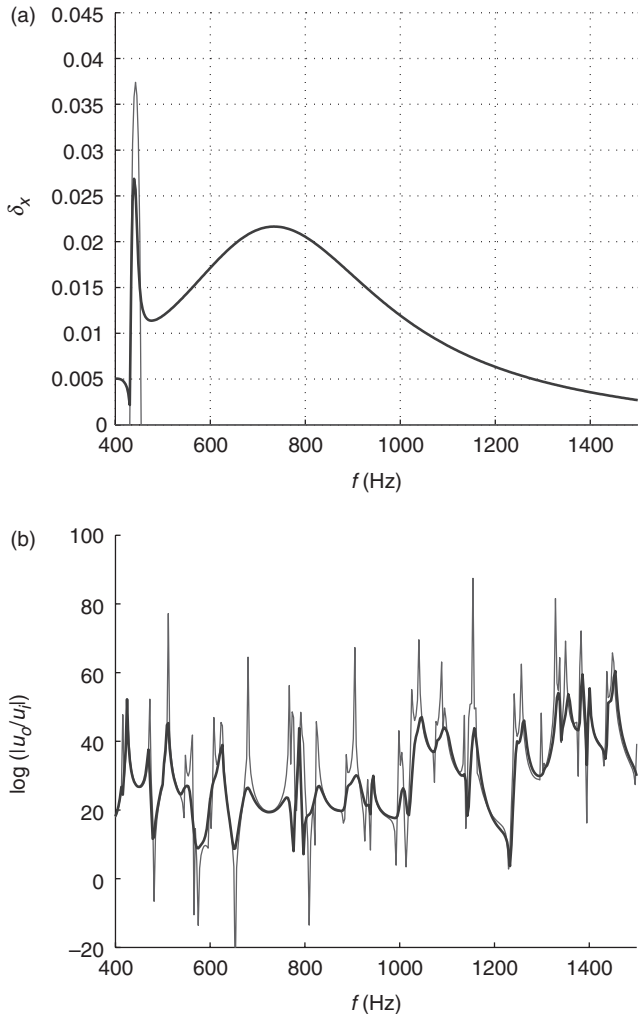

Figure 10. *Propagation constant (a) and frequency response function (b) with tuning at 850 Hz (tuning inductance L = 1.67 H): open circuit – thin solid line, shunting resistance R = 6000Ω – thick solid line.*

For reference purposes, the frequency response of the finite plate is complemented with the attenuation constants obtained for the corresponding shunting circuit configurations to show the consistency between the predictions of the unit cell analysis and the response of a finite assembly.

Specifically, Figures 9 and 10 compare the response obtained for tuning at 850 Hz and different values of shunting resistance. The frequency-response-function plots illustrate how vibration attenuation is achieved in the frequency range predicted by the unit cell analysis, and that the amount of attenuation is influenced by the shunting resistance. The difference can be observed through careful observation of the response amplitudes at the peak value of the attenuation constant. Figures 11 and 12 present examples of attenuation constants and frequency response obtained for tuning, respectively, at 650 and 1100 Hz. Both results confirm the ability of the periodic, shunted array to

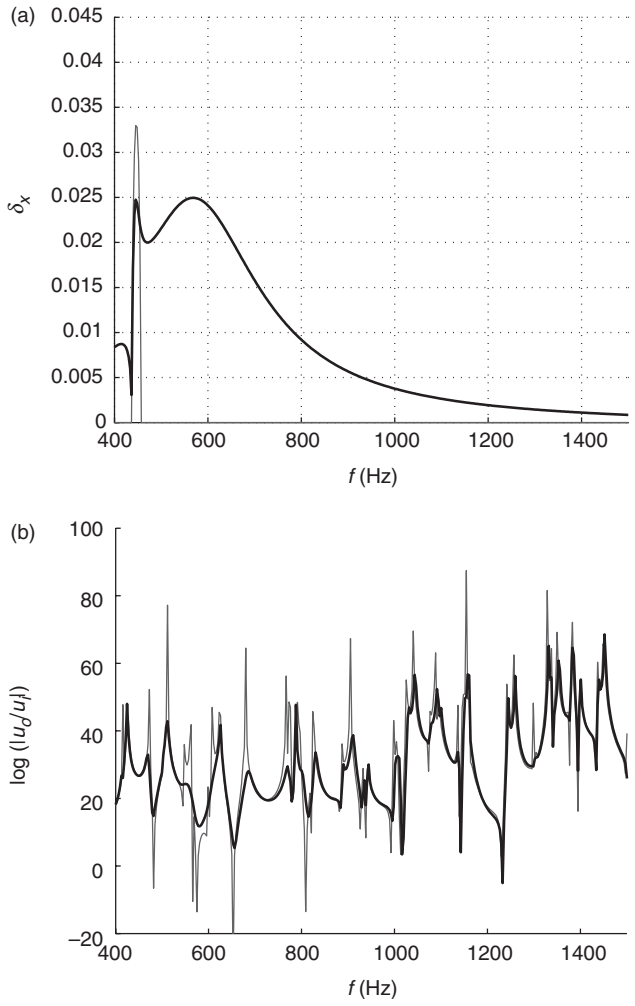

Figure 11. *Propagation constant (a) and frequency response function (b) for tuning at 650 Hz (tuning inductance $L = 2.85$ H, shunting resistance $R = 3000\ \Omega$).*

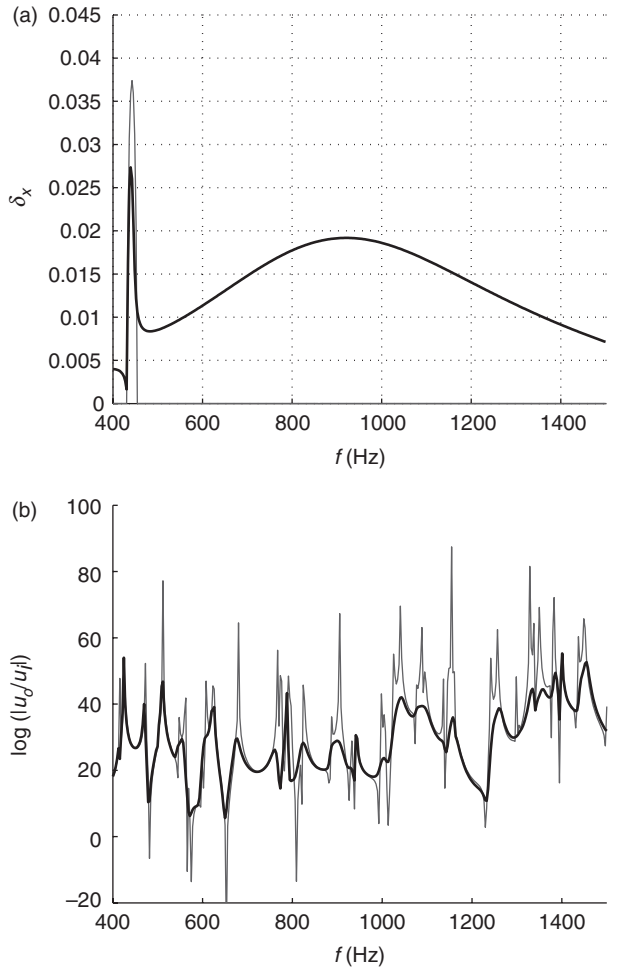

Figure 12. *Propagation constant (a) and frequency response function (b) for tuning at 1100 Hz (tuning inductance $L = 0.99$ H, shunting resistance $R = 3000\ \Omega$).*

reduce the amplitudes of all the modes contained in the frequency range of attenuation. Tuning at 1100 Hz in particular is characterized by a very significant broadband effect, while the results for 650 Hz show localized effectiveness around the tuning frequency. This is to be attributed to the characteristics of the resonant peak for the considered shunting circuits, whose bandwidth increases with the resonant frequency. The resonance behavior of the circuit and the equivalent effects on the structural-dynamics behavior of the system are also responsible for the shift between tuning frequency and the actual peak observed in all attenuation constants. In all the cases presented, in fact, one can clearly observe that maximum attenuation occurs at frequencies, which are lower than the tuned frequency for the shunt. This is due to two factors. First, the calculated tuning frequency is based on the resonant frequency of the circuit without dissipation, i.e., $\omega_{\mathrm{TUN}} = 1/\sqrt{\mathrm{LC}_p}$, while all considered shunting circuits feature a resistor R, which causes the shunting-circuit response to peak at its damped natural frequency. A second, and most important factor, consists in the fact that maximum effects of shunting on structural behavior are not achieved at the frequency for which electrical impedance $Z_e(\omega)$ is maximized, but rather at the value corresponding to a maximum of the shunting matrix $\boldsymbol{S}_{Z_e}(\omega)$ defined in Equation (15).

CONCLUSIONS

This article presents the analysis of wave propagation and subsequent vibrations in plates with periodic, shunted, piezoelectric patches. Finite element models are formulated to predict the wave propagation characteristics of the plate with piezo patches through the application of Bloch theorem on a unit cell of the periodic assembly. The formulation is general as it allows accommodating various structural and shunting configurations. The unit cell analysis gives the dispersion relations for the plate with shunted patches, which show the existence of ranges of frequency within which waves are attenuated as they propagate from one cell to another. Examples presented for two unit cell

configurations show that the presence of the shunted piezoelectric-patch arrays introduces an attenuation range due to the added mass and stiffness, and a second attenuation range which is defined by the parameters of the shunting circuit. This second attenuation zone is characterized by broadband behavior and can be tuned through the selection of the shunting circuit resonance characteristics. The attenuation effects of the periodic shunted array are demonstrated by computing the response of finite plate with a 5×5 piezo patch array, and by comparing the obtained range of attenuation with the one predicted by the unit cell analysis. The results show the consistency of the results, and suggest the effectiveness of the unit cell analysis as a design tool for the selection of array configuration, spatial periodicity and shunting configuration. The results also illustrate the strong broadband characteristics of the considered concept, which is contrast with the narrow-band effect obtained with a single patch shunted through an RL circuit.

ACKNOWLEDGMENTS

This work is supported by a collaborative research agreement (NNX07AD20A) between NASA Langley Research Center and the Georgia Institute of Technology.

APPENDIX: PERIODICITY CONDITIONS CORRESPONDING TO THE *FIRST BRILLOUIN ZONE*

The following describes the periodicity conditions and the degrees of freedom selected to define a transfer matrix corresponding to the 4 sides of the contour of the *First Brillouin Zone*. The first segment, already described in the body of the article, is included here for completeness.

Segment 1: $(0,0) - (\pi,0)$

It corresponds to $\mu_y = 0$. The periodicity conditions reduce to:

$$\begin{aligned} \boldsymbol{d}_T &= \boldsymbol{d}_B, \\ \boldsymbol{d}_{LT} &= \boldsymbol{d}_{LB}, \\ \boldsymbol{d}_{RT} &= \boldsymbol{d}_{RB}, \end{aligned}$$

Left, right and internal degrees of freedom are defined as:

$$\begin{aligned} \boldsymbol{d}_{\mathcal{L}} &= \{\boldsymbol{d}_L \quad \boldsymbol{d}_{LB}\}^T, \\ \boldsymbol{d}_{\mathcal{R}} &= \{\boldsymbol{d}_R \quad \boldsymbol{d}_{RB}\}^T, \\ \boldsymbol{d}_{\mathcal{I}} &= \{\boldsymbol{d}_B \quad \boldsymbol{d}_I\}^T. \end{aligned}$$

Segment 2: $(\pi,0) - (\pi,\pi)$

It corresponds to $\mu_x = \pi$. The periodicity conditions reduce to:

$$\begin{aligned} \boldsymbol{d}_R &= -\boldsymbol{d}_L, \\ \boldsymbol{d}_{RB} &= -\boldsymbol{d}_{LB}, \\ \boldsymbol{d}_{RT} &= -\boldsymbol{d}_{LT}, \end{aligned}$$

Left, right and internal degrees of freedom are defined as:

$$\begin{aligned} \boldsymbol{d}_{\mathcal{L}} &= \{\boldsymbol{d}_B \quad \boldsymbol{d}_{LB}\}^T, \\ \boldsymbol{d}_{\mathcal{R}} &= \{\boldsymbol{d}_T \quad \boldsymbol{d}_{LT}\}^T, \\ \boldsymbol{d}_{\mathcal{I}} &= \{\boldsymbol{d}_L \quad \boldsymbol{d}_I\}^T. \end{aligned}$$

Segment 3: $(\pi,\pi) - (0,\pi)$

It corresponds to $\mu_y = \pi$. The periodicity conditions reduce to:

$$\begin{aligned} \boldsymbol{d}_T &= -\boldsymbol{d}_B, \\ \boldsymbol{d}_{LT} &= -\boldsymbol{d}_{LB}, \\ \boldsymbol{d}_{RT} &= -\boldsymbol{d}_{RB}, \end{aligned}$$

Left, right and internal degrees of freedom are defined as:

$$\begin{aligned} \boldsymbol{d}_{\mathcal{L}} &= \{\boldsymbol{d}_L \quad \boldsymbol{d}_{LB}\}^T, \\ \boldsymbol{d}_{\mathcal{R}} &= \{\boldsymbol{d}_R \quad \boldsymbol{d}_{RB}\}^T, \\ \boldsymbol{d}_{\mathcal{I}} &= \{\boldsymbol{d}_R \quad \boldsymbol{d}_I\}^T. \end{aligned}$$

Segment 4: $(0,\pi) - (0,0)$

It corresponds to $\mu_x = 0$. The periodicity conditions reduce to:

$$\begin{aligned} \boldsymbol{d}_R &= \boldsymbol{d}_L, \\ \boldsymbol{d}_{RB} &= \boldsymbol{d}_{LB}, \\ \boldsymbol{d}_{RT} &= \boldsymbol{d}_{LT}, \end{aligned}$$

Left, right and internal degrees of freedom are defined as:

$$\begin{aligned} \boldsymbol{d}_{\mathcal{L}} &= \{\boldsymbol{d}_B \quad \boldsymbol{d}_{LB}\}^T, \\ \boldsymbol{d}_{\mathcal{R}} &= \{\boldsymbol{d}_T \quad \boldsymbol{d}_{LT}\}^T, \\ \boldsymbol{d}_{\mathcal{I}} &= \{\boldsymbol{d}_L \quad \boldsymbol{d}_I\}^T. \end{aligned}$$

REFERENCES

Becker, J., Fein, O., Maess, M. and Gaul, L. 2006. "Finite Element-based Analysis of Shunted Piezoelectric Structures for Vibration Damping," *Computers and Structures*, 84(31–32):2340–2350.

Behrens, S., Fleming, A.J. and Moheimani, S.O.R. 2002. "Series-parallel Impedance Structure for Piezoelectric Vibration Damping," In: *Proceedings of SPIE*, 4934:12.

Behrens, S. and Moheimani, S.O.R. 2000. "Optimal Resistive Elements for Multiple Mode Shunt-damping of a Piezoelectric Laminated Beam," *IEEE Conference on Decision and Control*, 4:4018–4023.

Brillouin, L. 1953. *Wave Propagation in Periodic Structures*, Dover, New York.

Clark, W.W. 2000. "Vibration Control with State-switched Piezoelectric Materials," *Journal of Intelligent Material Systems and Structures*, 11(4):263–271.

Cook, R.D., Malkus, D.S., Plesha, M.E. and Witt, R.J. 2007. *Concepts and Applications of Finite Element Analysis*, John Wiley & Sons, New York.

Corr, L.R. and Clark, W.W. 2001. "Piezoceramic Springs for Structural Semi-active Multi-modal Vibration Control," In: *Proceedings of the ASME Design Engineering Technical Conference*, Pittsburg, PA, 6 B:1343–1351.

Forward, R.L. 1979. "Electronic Damping of Vibrations in Optical Structures," *Applied Optics*, 18(5):690–697.

Hagood, N.W. and Von Flotow, A. 1991a. "Damping of Structural Vibrations with Piezoelectric Materials and Passive Electrical Networks," *Journal of Sound and Vibration*, 146(2):243–268.

Hagood, N.W. and Von Flotow, A. 1991b. "Hybrid Composites with Shunted Piezoelectric Particles for Vibration Damping," *Journal of Sound and Vibration*, 146(2):243–268.

Hollkamp, J.J. 1994. "Multimodal Passive Vibration Suppression with Piezoelectric Materials and Resonant Shunts," *Journal of Intelligent Material Systems and Structures*, 5(1):49–57.

Mead, D.J. 1996. "Wave Propagation in Continuous Periodic Structures: Research Contributions from Southampton 1964–1995," *Journal of Sound and Vibration*, 190(3):495–524.

Moheimani, S.O.R. and Behrens, S. 2004. "Multimode Piezoelectric Shunt Damping with a Highly Resonant Impedance," *IEEE Transactions on Control Systems Technology*, 12(3):484–491.

Moheimani, S.O.R., Fleming, A.J. and Behrens, S. 2001. "Highly Resonant Controller for Multimode Piezoelectric Shunt Damping," *Electronics Letters*, 37(25):1505–1506.

Moheimani, S.O.R., Fleming, A.J. and Behrens, S. 2004. "Dynamics, Stability, and Control of Multivariable Piezoelectric Shunts," *IEEE/ASME Transactions on Mechatronics*, 9(1):87–99.

Morgan, R.A. and Wang, K.W. 2000. "An Active-passive Piezoelectric Vibration Absorber for Structural Control Under Harmonic Excitations with Time-varying Frequency," *American Society of Mechanical Engineers, Aerospace Division (Publication) AD*, 60:285–297.

Neubauer, M. and Oleskiewicz, R. 2006. "Suppression of Brake Squeal using Shunted Piezoceramics," In: *Proceedings of 8th Biennial ASME Conference on Engineering Systems Design and Analysis, ESDA2006*, Torino, Italy, p. 10.

Park, C.H. and Baz, A. 2005. "Vibration Control of Beams with Negative Capacitive Shunting of Interdigital Electrode Piezoceramics," *JVC/Journal of Vibration and Control*, 11(3):331–346.

Tang, J. and Wang, K.W. 1999a "Vibration Control of Rotationally Periodic Structures using Passive Piezoelectric Shunt Networks and Active Compensation," *Journal of Vibration and Acoustics, Transactions of the ASME*, 121(3):379–390.

Tang, J. and Wang, K.W. 1999b. "Vibration Control using Piezoelectric Material with High Order Nonlinearity," *American Society of Mechanical Engineers, Aerospace Division (Publication) AD*, 59:149–160.

Tang, J. and Wang, K.W. 2003. "Vibration Delocalization of Nearly Periodic Structures using Coupled Piezoelectric Networks," *Journal of Vibration and Acoustics, Transactions of the ASME*, 125(1):95–108.

Thorp, O., Ruzzene, M. and Baz, A. 2001. "Attenuation and Localization of Wave Propagation in Rods with Periodic Shunted Piezoelectric Patches," *Smart Materials and Structures*, 10(5):979–989.

Thorp, O., Ruzzene, M. and Baz, A. 2005. "Attenuation and Localization of Waves in Shells with Periodic Shunted Piezo Rings," *Smart Materials and Structures*, 14(4):594–604.

Tsai, M.S. and Wang, K.W. 1996. "Control of a Ring Structure with Multiple Active-passive Hybrid Piezoelectrical Networks," *Smart Materials and Structures*, 5(5):695–703.

Wu, S.-Y. 1999. "Method for Multiple Mode Piezoelectric Shunting with Single Pzt Transducer for Vibration Control," *Journal of Intelligent Material Systems and Structures*, 9(12):991–998.